Optical absorption and transmission in a molybdenum disulfide monolayer

Rukelj, Zoran; Štrkalj, Antonio; Despoja, Vito

Source / Izvornik: **Physical Review B, 2016, 94**

Journal article, Published version
Rad u časopisu, Objavljena verzija rada (izdavačev PDF)

https://doi.org/10.1103/PhysRevB.94.115428

Permanent link / Trajna poveznica: https://urn.nsk.hr/urn:nbn:hr:217:668545

Rights / Prava: In copyright / Zaštićeno autorskim pravom.

Download date / Datum preuzimanja: **2024-07-23**

Repository / Repozitorij:

Repository of the Faculty of Science - University of Zagreb

Optical absorption and transmission in a molybdenum disulfide monolayer

Zoran Rukelj,[1] Antonio Štrkalj,[1] and Vito Despoja[1,2]
[1]*Department of Physics, University of Zagreb, Bijenička 32, HR-10000 Zagreb, Croatia*
[2]*Donostia International Physics Center (DIPC), P. Manuel de Lardizabal, 20018 San Sebastian, Basque Country, Spain*
(Received 18 May 2016; revised manuscript received 21 August 2016; published 21 September 2016)

Our recently proposed theoretical formulation [presented in D. Novko *et al.*, Phys. Rev. B **93**, 125413 (2016)] is used to study optical absorption and transmission in molybdenum disulfide (MoS_2) monolayer as a function of incident photon energy and angle. The investigation is not focused on exploration of well-documented spin-orbit split excitons around optical absorption onset, but rather on the most intensive features in absorption spectrum in the visible and near-ultraviolet photon energy range (1.7–4 eV). It is shown that three most intensive peaks, at 2.7, 3.1, and 3.7 eV, result from transitions between Mo(d) and S(p) valence and conduction bands and that the character of their charge/current density fluctuations is intrinsically in plane, located in the molybdenum plane. This also implies that MoS_2 monolayer is completely transparent when illuminated by grazing incidence p-polarized light. The validity of the presented results is supported by our effective two-band tight-binding model and finally by good agreement with some recent experimental results.

DOI: 10.1103/PhysRevB.94.115428

I. INTRODUCTION

Intensive research of graphene [1] is getting saturated and there is a need for other quasi-two-dimensional (q2D) materials which would be complementary to graphene in the way that they can improve its shortcomings. The lack of natural band gap and low optical absorption in the visible light range make graphene unsuitable for developing optoelectronic and photovoltaic devices [2–4]. Also, the two-dimensional plasmon-polariton (2DPP) mode in doped graphene is strongly damped, diminishing graphene's ability to serve as information carrier [5], or as an active material in chemical sensing [6], due to the very low oscillator strength of the mode. However, a combination of graphene and other q2D materials can improve their common characteristics significantly. The best candidates are q2D materials with natural band gap, such as molybdenum disulfide (MoS_2) [7,8] or hexagonal boron nitride (h-BN) [9–11]. Heterostructures which are combinations of graphene monolayer and MoS_2 or BN monolayers have recently been fabricated and investigated [12]. Researchers from MIT developed a new solar cell made of graphene and MoS_2 [13], where graphene low absorption and good conductivity enabled it to serve as transparent electrode, while MoS_2, being a good absorber (in visible region), serves as optically active material.

In this paper, we use our recently proposed theoretical formulation [14] to investigate angle-resolved optical absorption and transmission in MoS_2. We also make a brief comparison with the optical properties in graphene, studied in detail in other theoretical and experimental investigations [4,15–18]. This theory is based on calculation of current-current response tensor $\Pi_{\mu\nu}$ within random phase approximation (RPA), where the electromagnetic interaction is mediated by free photon propagator $D^0_{\mu\nu}$. The tensorial character of the theory allows us to analyze the response to transverse electric [s(TE)] and response to transverse magnetic [p(TM)] external electromagnetic field and to analyze how optical properties of q2D depend on external electromagnetic field incident angle. The formulation also includes effects of retardation which can strongly influence the dispersion relations of plasmon-polariton (PP) modes in metallic and doped semiconductor systems. The optical properties of MoS_2 are also studied by using effective two-band tight-binding model (2B-TBA), which allows easier classification of the features in optical spectrum. The disadvantage of this formulation is its inability to provide electron-hole bound state or excitons in semiconducting q2D such as MoS_2. However, there are many other, very sophisticated, theoretical studies of optical properties in MoS_2 [19,20] which include quasiparticles GW correction as well as solution of Bethe-Salpeter equation (BSE) or so called GW-BSE scheme [21–23]. These calculations provide excitonic features in optical spectra which are in very good agreement with available experimental results [7,8,24].

This investigation is not focused on investigation of excitons, which constitute only a tiny part of the optical spectra, but rather on all other features which appear in visible photon energy range ($1.5 < \hbar\omega < 4$ eV) of optical spectra. We also show that our simple 2B-TBA model gives realistic description of optical absorption spectra, which helps us to understand the origin of particular features, such as the position of various peaks in the spectra and their dependence on the interband relaxation constant. Optical properties are probed with electromagnetic waves with different incident angles, which allows us to understand the spatial distribution of the induced charge or current density oscillations.

In Sec. II A, we briefly present geometry of the system and formulation of optical absorption and transmission in terms of *ab initio* current-current response tensor $\Pi^0_{\mu\nu}$, as well as our 2D-TBA model. In Sec. III, we analyze optical absorption of p-polarized normal incidence ($\theta = 0$) light, and compare it with results of TBA model and with some recent experimental results. We then analyze the optical absorbance and transmittance of p-polarized light in MoS_2 monolayer as function of incident angle θ and photon energy $\hbar\omega$. We also make a brief comparison with the angle-resolved optical absorption in graphene. In Sec. IV, we present our conclusion.

II. FORMULATION OF THE PROBLEM

A. Optical absorption and transmission

In order to formulate the scattering of plane electromagnetic wave on q2D crystal, we start from steps that have already been

 ©2016 American Physical Society

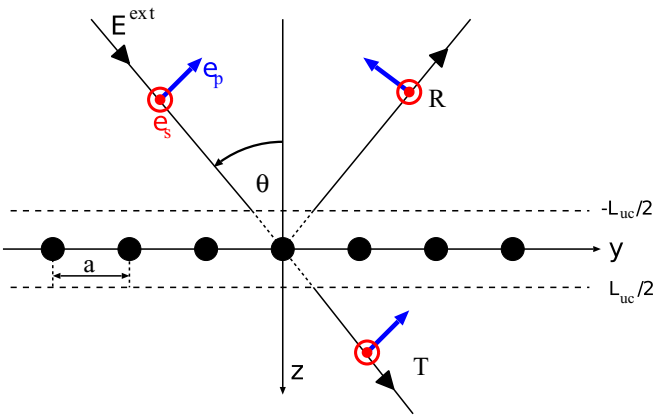

FIG. 1. Schematic description of the geometry of the system. The q2D crystal lies in the x-y plane, a represents lattice constant in the x-y plane and L_{uc} is the lattice constant in the z direction. θ is incident angle of s(TE) and p(TM) polarized electromagnetic field.

thoroughly derived in our previous work [14,25], and derive expressions for angle-resolved absorbance and transmittance.

Our system, schematically shown in Fig. 1, consists of a q2D crystal (crystal slab) parallel to the x-y plane, with charge and current density fluctuations occupying the region $z \in [\frac{-L_{uc}}{2}, \frac{L_{uc}}{2}]$. The incident electromagnetic field is a plane wave of unit amplitude

$$\mathbf{E}^{\text{ext}}_{s,p}(\mathbf{r},t) = \mathbf{e}^{s,p} e^{iQy+i\beta z} e^{-i\omega t}, \tag{1}$$

where $\mathbf{e}^s = (1 \quad 0 \quad 0)$ and $\mathbf{e}^p = (0 \quad \cos\theta \quad -\sin\theta)$ represent polarization of s(TE) and p(TM) electromagnetic waves, respectively. θ is incident angle with respect to negative $-z$ axis, $\sin\theta = \frac{Qc}{\omega}$, $\cos\theta = \frac{\beta c}{\omega}$, $\omega = kc$, and $k = \sqrt{Q^2+\beta^2}$.

The incident electromagnetic field interacts with charge/current density fluctuations in the crystal slab and the total electromagnetic field can be written as

$$\mathbf{E}(\mathbf{r},t) = \mathbf{E}^{\text{ext}}(\mathbf{r},t) + \mathbf{E}^{\text{scatt}}(\mathbf{r},t), \tag{2}$$

where the scattered electromagnetic field (in $\Phi = 0$ gauge) can be written as

$$\mathbf{E}^{\text{scatt}}(\mathbf{r},t) = -\frac{1}{c}\frac{\partial}{\partial t}\int dt_1 dt_2 \int d\boldsymbol{\rho}_1 d\boldsymbol{\rho}_2 \int_{-L_{uc}/2}^{L_{uc}/2} dz_1 dz_2 \times \hat{\mathbf{D}}_0(\mathbf{r},\mathbf{r}_1,t-t_1)\hat{\Pi}(\mathbf{r}_1,\mathbf{r}_2,t_1-t_2)\mathbf{A}^{\text{ext}}(\mathbf{r}_2,t_2). \tag{3}$$

Here, $\hat{\mathbf{D}}_0$ is free photon propagator, $\hat{\Pi}$ is current-current response tensor of the crystal slab, $\mathbf{A}^{\text{ext}} = -c\int^t dt' \mathbf{E}^{\text{ext}}(t')$ is the incident vector potential, and $\boldsymbol{\rho} = (x,y)$ is the radius vector in the x-y plane so that the 3D radius vector can be written as $\mathbf{r} = (\boldsymbol{\rho},z)$. All quantities denoted as $\hat{\mathbf{T}}$ represent tensors, i.e., 3×3 matrices $T_{\mu\nu}$; $\mu\nu = x,y,z$. In the optical limit, $Q \ll 1/a$, where a is the unit-cell constant (as sketched in Fig. 1), it is fully justified to ignore the crystal local field effects in the x-y plane. In that case, the current-current response tensor Π can be Fourier expanded as

$$\hat{\Pi}(\mathbf{r},\mathbf{r}',t-t') = \frac{1}{L_{uc}}\sum_{G_z G_z'} e^{iG_z z - iG_z' z'} \int \frac{d\omega}{2\pi} e^{-i\omega(t-t')} \times \int \frac{d\mathbf{Q}}{(2\pi)^2} e^{i\mathbf{Q}(\boldsymbol{\rho}-\boldsymbol{\rho}')}\, \hat{\Pi}_{G_z,G_z'}(\mathbf{Q},\omega), \tag{4}$$

where G_z are reciprocal lattice vectors in direction perpendicular to the slab, and $\mathbf{Q} = (Q_x, Q_y)$ is wave vector in the x-y plane. In this case, it is also convenient to perform partial Fourier expansion (z remains untransformed) of free photon propagator

$$\hat{\mathbf{D}}^0(\mathbf{r},\mathbf{r}_1,t-t') = \int \frac{d\omega}{2\pi} e^{-i\omega(t-t')} \times \int \frac{d\mathbf{q}}{(2\pi)^2} e^{i\mathbf{Q}(\boldsymbol{\rho}-\boldsymbol{\rho}')}\, \hat{\mathbf{D}}^0(\mathbf{Q},\omega,z,z'). \tag{5}$$

Since we assume the isotropy in the crystal (x-y) plane, it is sufficient to analyze only one $\mathbf{q}$ direction, and we choose that to be the y direction (the direction of incident electromagnetic field). In that case, the Fourier transform of free photon propagator can be explicitly written as 3×3 matrix presented in Appendix A [25].

After inserting (1), expansions (4) and (5), and definitions (A2)–(A5) in (3), the scattered or "reflected" electromagnetic field in the region $z < -L_{uc}/2$ can be written as

$$\mathbf{E}^{\text{scatt}}_s(\boldsymbol{\rho},z<-L_{uc}/2,t) = R_s \begin{pmatrix}1\\0\\0\end{pmatrix} e^{i(Qy-\beta z-\omega t)} \tag{6}$$

and

$$\mathbf{E}^{\text{scatt}}_p(\boldsymbol{\rho},z<-L_{uc}/2,t) = R_p \begin{pmatrix}0\\\cos\theta\\\sin\theta\end{pmatrix} e^{i(Qy-\beta z-\omega t)}. \tag{7}$$

Here, the amplitude of reflected s wave is

$$R_s = \frac{2\pi i}{c\beta} D_{xx}(\mathbf{Q},\omega), \tag{8}$$

and the amplitude of reflected p wave is

$$R_p = \frac{2\pi i}{\omega}[D_{yy}(\mathbf{Q},\omega)\cos\theta - D_{zz}(\mathbf{Q},\omega)\sin\theta\tan\theta], \tag{9}$$

where we introduce the surface electromagnetic field propagator

$$D_{\mu\nu}(\mathbf{Q},\omega) = \sum_{G_z G_z'} I^+_{G_z} \Pi_{\mu\nu,G_z,G_z'}(\mathbf{Q},\omega) I^-_{G_z'},$$

and where the form factors are

$$I^{\pm}_{G_z} = \frac{2}{\sqrt{L}}\frac{\sin[(\beta \pm G_z)L_{uc}/2]}{\beta \pm G_z}.$$

The reflected electromagnetic field energy flux (Poynting vector) in the direction perpendicular to crystal surface, normalized to incident flux $\mathcal{P}_{\text{ext}} = \frac{c}{8\pi}$, is $\mathcal{R} = 2[\mathbf{E}\times\mathbf{B}]_z$. After using $\mathbf{B} = \nabla\times\mathbf{A}$, $\mathbf{A} = -c\int^t dt' \mathbf{E}(t')$ and $\mathbf{E} = \{\mathbf{E}^{\text{scatt}} + [\mathbf{E}^{\text{scatt}}]^*\}/2$, and time averaging, the reflected energy

flux becomes

$$\mathcal{R}_{s,p} = |R_{s,p}|^2. \tag{10}$$

As shown before [14], the normalized absorption power per unit area is given by

$$\mathcal{A}_{s,p} = \frac{4\pi}{\omega} S(\mathbf{Q},\omega), \tag{11}$$

where spectral function is

$$S_{s,p}(\mathbf{Q},\omega) = \mathrm{Im}\left\{ \sum_{\mu,\nu} e_{\mu}^{s,p} e_{\nu}^{s,p} \sum_{G_z,G_z'} I_{G_z}^{+} \Pi_{\mu\nu,G_zG_z'}(\mathbf{Q},\omega) I_{G_z'}^{+} \right\}.$$

The transmitted electromagnetic energy flux can be obtained by using the energy conservation law

$$\mathcal{T}_{s,p} = 1 - \mathcal{R}_{s,p} - \mathcal{A}_{s,p}. \tag{12}$$

The main quantity appearing in the above expressions for absorbance, reflectivity, and transmittance (10)–(12) is the screened current-current response tensor $\Pi_{\mu\nu}$, and the method we use to obtain it is described in Appendix B.

B. Band-structure calculation

In order to anticipate the contribution of various electronic excitations to various features in the optical absorption (or transmission), we first analyze the orbitally decomposed MoS_2 band structure and then use the obtained conclusions to construct effective two-band TBA model, which helps us to identify the particular peaks in the absorption spectra.

For calculation of the MoS_2 ground-state band structure, we use plane-wave self-consistent field DFT code (PWSCF) within QUANTUM ESPRESSO(QE) package [26]. The core-electron interaction is approximated by the norm-conserving pseudopotentials [27], and the exchange correlation (XC) potential by the Perdew-Zunger local density approximation (LDA) [28]. The ground-state electronic densities of MoS_2 monolayer (ML) are calculated by using $12\times12\times1$ Monkhorst-Pack K-point mesh [29] of the first Brillouin zone (BZ), and for the plane-wave cutoff energy we choose 50 Ry (680 eV). For MoS_2-ML unit-cell constant we use the experimental value of $a = 5.972$ a.u. and the vertical separation between sulfur layers is 5.868 a.u. [30]. The neighboring MoS_2-MLs (in supercell) are separated by the distance $L_{uc} = 5a = 29.86$ a.u. The MoS_2 band structure along the high-symmetry Γ-K-M-Γ directions is calculated along the path with 201 k points.

Because the main features in absorption spectra come from the transition between several bands below Fermi energy and several bands above Fermi energy, here we first define the name of such bands in order to reduce confusion when we refer to them. The highest valence band and the lowest conduction band we call just valence and conduction bands, respectively. The next band lower in energy than valence band we call second valence band, the next lower band we call third valence band, and so on. Similarly, the next band upper in energy than conduction band we call second conduction band, the next upper band we call third conduction band, and so on.

Figure 2 shows the intensities of contributions of the molybdenum 4[d_{xz}, d_{yz}, d_{z^2}, d_{xy}, and $d_{x^2-y^2}$] orbitals (left panel), denoted as Mo(d), and sulfur 3[p_x, p_y] orbitals (right panel), denoted as S(p), to the MoS_2 band structure. The intensities of Mo(s), Mo(p), S(s), and S(d) orbitals are not shown because their contribution is negligible in the presented energy interval. The energy scale is aligned so that the Fermi energy is equal to zero.

We can see that the 1.78-eV LDA gap (direct gap at K point) almost coincides with the LDA gap reported in Ref. [19], but in that paper the authors reported that the quasiparticle (G_1W_0) correction increases the gap to 2.84 eV. Therefore, as expected in semiconductors or insulators, the LDA strongly underestimates the quasiparticle gap, which makes our RPA response theory based on LDA wave functions and energies inadequate. Fortunately, since optical gap (excitation gap)

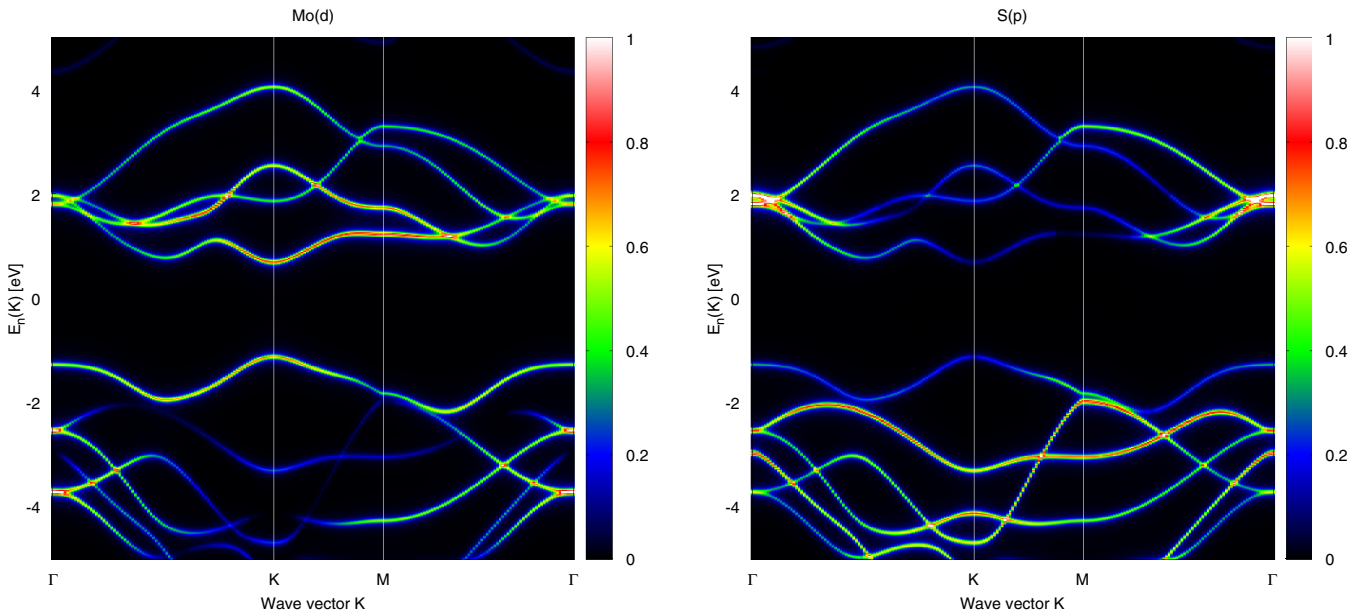

FIG. 2. The intensities of contributions of the Mo(d) orbital (left panel) and S(p) orbital (right panel) to MoS_2 band structure.

almost coincides with LDA gap (as reported in many theoretical and experimental papers [7,8,19,20,24,31]), it means that excitonic effect (electron-hole attraction), also not included in our RPA formulation, cancels the quasiparticle correction almost exactly. This cancellation should be taken with care because it could be valid only for valence and conductive bands around the K point, but our optical spectra indicate that it is valid for the majority of valence and conduction bands. Exclusion of electron-hole attraction also excludes A and B excitons [19] from the optical absorption spectra, but that part of the spectrum is not an objective of our research.

It can be noticed (in the right panel) that the second and third valence bands mainly consist of S(p) orbitals while (in left panel) second and third conduction bands mainly consist of Mo(d) orbitals. However, it can also be noticed the small but not negligible contribution of Mo(d) orbitals in the second and third valence bands and contribution of S(p) orbitals in the second and third conduction bands. It is also noticeable that the second valence band in the Γ-K direction has dominant S(p) character while the second conduction band around the M point has dominant Mo(d) character, etc. In the dipole approximation $k^{-1} \gg a$ (which is in our case completely justified), the electromagnetic field can, due to dipole matrix elements selection rules, cause transitions only between the states which angular momentum quantum numbers differ for one. Therefore, the above-described angular momentum composition of valence and conducting bands tells us that electromagnetic field will be capable to cause transition between them. Here, we are mostly interested in optical absorption in visible energy range, up to 4 eV, mainly contributed by transitions between conduction and valence bands.

C. Effective 2B-TBA model

High-quality image of electronic bands in MoS_2 can be obtained in the tight-binding approximation (TBA) with the nearest-neighbor hopping, taking into account a large number of atomic orbitals [32,33]. However, if we want a model more suitable for theoretical calculation of electronic properties for energies comparable with the gap, it is sufficient to limit the calculations to just a few bands. Keeping that in mind, we construct a two-band TBA model which captures all significant features of the valence bands.

As shown by DFT calculations, these bands are constructed mainly from S(p) and Mo(d) orbitals, and now we want to implement this property in the TBA model. To do that, it is helpful to view the system as one composed of Mo atom and S_2 molecule. Each sulfur molecule can be seen as a molecule with two effective molecular orbitals, one symmetric and one antisymmetric, which are linear combinations of atomic sp^2 hybrids. Since molybdenum is located in the middle layer, we can keep the overlap between molybdenum effective d orbital and the symmetric sulfur orbital as the most relevant parameter since the value of antisymmetric orbital vanishes in the middle plane. The price to pay for choosing this "effective" two-band model (where we have neglected effective asymmetric sulfur orbital) is the inclusion of electron hopping between the same orbitals in distant neighbors if we want to include, quantitatively and qualitatively, all significant features of both bands.

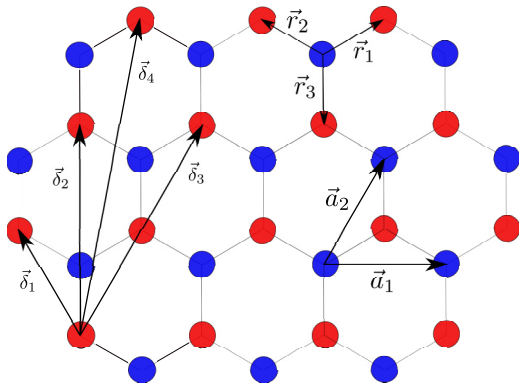

FIG. 3. A top view of MoS_2 plane with molybdenum atoms (red) and sulfur atoms (blue). $\mathbf{a}_1$ and $\mathbf{a}_2$ are primitive vectors. Distance to the four alike neighbors is shown.

1. Hamiltonian

To construct the TBA Hamiltonian, we label the sulfur and molybdenum orbitals with $\ell = \{s,m\}$ and define $c^\dagger_{\mathbf{R}\ell}$ as an electron creation operator in the ℓth orbital at position $\mathbf{r}_\ell$ in the unit cell with a Bravais vector $\mathbf{R}$. If we choose the primitive vectors to be $\mathbf{a}_1 = a(1,0)$ and $\mathbf{a}_2 = a(1/2,\sqrt{3}/2)$ ($a = 3.16$ Å) with the orbitals relative positions $\mathbf{r}_s = 0$ and $\mathbf{r}_m = \mathbf{r}_1 = (\mathbf{a}_1 + \mathbf{a}_2)/3$ as shown Fig. 3, the Hamiltonian is

$$\hat{H}_0 = \sum_{\mathbf{R},\boldsymbol{\delta}} \sum_{\ell\ell'} H_0^{\ell\ell'}(\boldsymbol{\delta} + \mathbf{r}_{\ell'\ell}) c^\dagger_{\mathbf{R}\ell} c_{\mathbf{R}+\boldsymbol{\delta}\ell'}. \tag{13}$$

The elements $H^{\ell\ell'}(\boldsymbol{\delta} + \mathbf{r}_{\ell'\ell})$ are binding energies associated with electron hopping processes between the two ℓ,ℓ' orbitals, depending solely on the distance between them. Vector $\boldsymbol{\delta}$ is the position of neighbor unit cells relative to $\mathbf{R}$, and $\mathbf{r}_{\ell'\ell} = \mathbf{r}_{\ell'} - \mathbf{r}_\ell$ is the distance between the two orbitals within the unit cell. By Fourier transforming the Hamiltonian (13),

$$\hat{H}_0 = \sum_{\mathbf{K}} \sum_{\ell\ell'} H_0^{\ell\ell'}(\mathbf{K}) c^\dagger_{\ell\mathbf{K}} c_{\ell'\mathbf{K}}, \tag{14}$$

we can define the matrix elements in a more familiar way. The diagonal elements are the sum of the onsite orbital energy ($\boldsymbol{\delta} = 0$) and the contribution from hopping to most alike neighbors at distance $\boldsymbol{\delta} > 0$. Since $\mathbf{r}_{\ell\ell} = 0$, we get

$$H_0^{\ell\ell}(\mathbf{K}) = \varepsilon_\ell(\mathbf{K}) = \varepsilon_\ell + \sum_{\boldsymbol{\delta}>0} 2t_{\ell\ell}(\boldsymbol{\delta})\cos(\mathbf{K}\cdot\boldsymbol{\delta}). \tag{15}$$

As for the nondiagonal elements, for example H_0^{sm}, we retain only the hopping to the three nearest neighbors located at $\mathbf{r}_1 = \mathbf{r}_{ms}$, $\mathbf{r}_2 = \mathbf{r}_{ms} - \mathbf{a}_1$, and $\mathbf{r}_3 = \mathbf{r}_{ms} - \mathbf{a}_2$ as shown schematically in Fig. 3. Therefore,

$$H_0^{sm}(\mathbf{K}) = t^*_{sm}(\mathbf{K}) = t_{sm} \sum_{j=1}^{3} e^{i\mathbf{K}\cdot\mathbf{r}_j}. \tag{16}$$

Note that the expression (16) is the usual parametrization of the off-diagonal part of TBA Hamiltonian in graphene or h-BN

TABLE I. $\delta \equiv |\boldsymbol{\delta}|$ is the distance to the neighbors and the t_{mm} and t_{ss} are the corresponding hopping parameters between the same orbitals. For example, there are six sulfur orbitals $|\boldsymbol{\delta}| = \sqrt{3}a$ away from the the sulfur orbital we choose as a reference one, at positions $\boldsymbol{\delta} = \pm(2\mathbf{a}_2 - \mathbf{a}_1)$, $\pm(2\mathbf{a}_1 - \mathbf{a}_2)$, $\pm(\mathbf{a}_2 + \mathbf{a}_1)$, to which the electron hopping parameter is the same $t_{ss} = 15$ meV.

δ	a	$\sqrt{3}a$	$2a$	$\sqrt{7}a$	$3a$	$2\sqrt{3}a$	$\sqrt{13}a$	$4a$
t_{ss}/meV	45	15	60	0	5	−35	5	15
t_{mm}/meV	20	100	10	−5	−5	10	0	−5
$\varepsilon_m = 1.15$ eV $\varepsilon_s = -1.7$ eV $t_{sm} = 0.3$ eV								

with a well-known dispersion [34,35]

$$|t_{sm}(\mathbf{K})| = \sqrt{3 + 2\cos K_x a + 4\cos\frac{K_x a}{2}\cos\frac{\sqrt{3}K_y a}{2}}. \quad (17)$$

Hamiltonian (14) can be diagonalized by unitary transformation, as shown in Appendix D, with the eigenvalues

$$E_{\pm}(\mathbf{K}) = \frac{\varepsilon_m(\mathbf{K}) + \varepsilon_s(\mathbf{K})}{2} \pm \frac{1}{2}\sqrt{[\varepsilon_m(\mathbf{K}) - \varepsilon_s(\mathbf{K})]^2 + 4|t_{sm}(\mathbf{K})|^2}. \quad (18)$$

The elements of (15) and (16) like atomic orbital energies ε_s and ε_m, hopping parameters t_{mm}, t_{ss}, and t_{sm} are found by using the method of least squares, that is, by requiring that the difference of squares between the valence bands obtained from the first principles (Fig. 2) and the expression (18) for arbitrary chosen points in the Brillouin zone is minimal. The parameters are given in Table I and the dispersions (18) are shown in Fig. 4.

2. *Interaction with external field and the dynamical conductivity tensor*

In the tight-binding approximation, the coupling between valence electrons and the electromagnetic field given by a vector potential $\mathbf{A}(\mathbf{r},t)$ is described by Peierls substitution [36] in the bare Hamiltonian (13). That way, we obtain $\hat{H}_{\text{tot}}$, as shown in Appendix C, and the coupling Hamiltonian is defined as $\hat{H}_{\text{ext}} = \hat{H}_{\text{tot}} - \hat{H}_0$. For sufficiently small fields, we can expand $\hat{H}_{\text{tot}}$ in powers of $\mathbf{A}(\mathbf{r},t)$ and keep only the linear term to obtain

$$\hat{H}_{\text{ext}} = -\frac{1}{c}\sum_{\mathbf{Q},\mu} A_\mu(\mathbf{Q},t)\hat{J}^{\text{para}}_\mu(-\mathbf{Q}). \quad (19)$$

In (19), we have identified the paramagnetic current operator and introduced Cartesian coordinates μ. For further calculations it is useful to present the paramagnetic current operator in diagonal representation:

$$\hat{J}^{\text{para}}_\mu(\mathbf{Q}) = \sum_{LL'}\sum_{\mathbf{K}} J^{LL'}_\mu(\mathbf{K},\mathbf{K}+\mathbf{Q}) c^\dagger_{L\mathbf{K}} c_{L'\mathbf{K}+\mathbf{Q}}, \quad (20)$$

with the matrix elements $J^{LL'}_\mu(\mathbf{k},\mathbf{k}+\mathbf{Q})$ given in Appendix D. The diagonal conductivity tensor is given by a well-known expression [34]

$$\sigma_{\mu\mu}(\mathbf{Q},\omega) = \frac{i}{\omega}[\Pi_{\mu\mu}(\mathbf{Q},\omega) - \Pi_{\mu\mu}(\mathbf{Q},0)], \quad (21)$$

where we have defined

$$\Pi_{\mu\mu}(\mathbf{Q},\omega) = \int_0^\beta d\tau\, e^{i\omega\tau}\left\langle T_\tau \hat{J}^{\text{para}}_\mu(\mathbf{Q},\tau)\hat{J}^{\text{para}}_\mu(-\mathbf{Q},0)\right\rangle \quad (22)$$

as Matsubara current-current correlation function for the homogeneous and isotropic system with the current operators (20). The static part of the correlation function is related to the diamagnetic contribution to the conductivity and, using continuity equation, it can be shown that it is given by the effective number of charge carriers $\Pi_{\mu\mu}(\mathbf{Q},0) = e^2 n_{\mu\mu}(\mathbf{Q})/m$. Since this term is real, it gives no contribution to the real part of conductivity. After performing analytical continuation of expression (22), and introducing interband relaxation time approximation by changing $i\eta \to i\hbar\gamma$, where the relaxation constant γ is connected with the relaxation time τ_r in the usual way $\gamma = 1/\tau_r$, we obtain

$$\Pi_{\mu\mu}(\mathbf{Q}\approx 0,\omega) = \frac{1}{V}\sum_{\mathbf{K},\sigma,L\neq L'} \left|J^{LL'}_\mu(\mathbf{K})\right|^2 \times \frac{f_L(\mathbf{K}) - f_{L'}(\mathbf{K})}{\hbar\omega + E_L(\mathbf{K}) - E_{L'}(\mathbf{K}) + i\hbar\gamma}. \quad (23)$$

Since we are studying optical transitions, we are interested in the interband conductivity in the $\mathbf{Q}\approx 0$ limit.

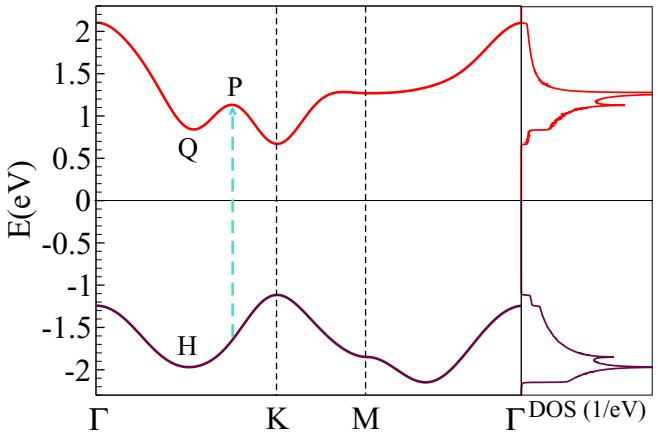

FIG. 4. The valence band (violet) and conduction band (red) and their density of states (right panel). Notice the saddle points at P, H and M which give singular contribution to the density of states. The points Q and H are approximately at $(2\pi/3a,0)$ as noted in Ref. [32].

III. RESULTS AND DISCUSSION

A. Optical absorption in MoS_2

Let us first analyze the optical absorbance calculated using (11) with current-current response tensor $\Pi^0_{\mu\nu}$ [Eq. (B3)]. The $\Pi^0_{\mu\nu}$ is calculated from the Kohn-Sham (KS) wave functions $\phi_{L\mathbf{K}}(\mathbf{r})$ and energies $E_L(\mathbf{K})$ obtained by the ground-state calculation, as described in Sec. II B. In the summation over $\mathbf{K}$ in (B3) we use $201\times201\times1$ K-point mesh sampling, which corresponds to 40 405 Monkhorst-Pack special k points in the Brillouin zone and 6835 points in the irreducible Brillouin zone. Band summation (L,L') in (B3) is performed

over 50 bands and we use damping parameter $\eta = 50$ meV. Broken symmetry in the z direction results in significant inhomogeneity of induced current and charge densities in that direction. This requires inclusion of the crystal local field effects in the z direction, which is achieved by using 61 G_z Fourier components, corresponding with 20 Ry (544 eV) crystal local field effects cut off. After solving the Dyson equation (B1) we obtain the screened current-current response tensor $\hat{\mathbf{\Pi}}$, which can be inserted in the expression for the optical absorbance (11) or the expression for transmittance (12). The validity of RPA result is tested by the f-sum rule check

$$\frac{2m}{\pi e^2}\int_0^\infty d\omega\, \mathrm{Re}\sigma_{\mu\mu}(\omega) = N_{el};\ \mu = x,y$$

where $N_{el} = 18$ is the number of electrons per unit cell and the conductivity is calculated as $\mathrm{Re}\sigma_{\mu\mu}(\omega) = \frac{1}{\omega}\mathrm{Im}\Pi^0_{\mu\mu,G_z=0,G'_z=0}(\mathbf{Q}=0,\omega)$. We found that described parameters give satisfactory 4% f-sum rule error. Results for optical absorption can be compared with optical conductivity in our 2B-TBA model (23) and with some recent experimental results.

The black solid line in Fig. 5(a) shows the RPA result [obtained from Eq. (11)] for optical absorbance of p-polarized normal incidence ($\theta = 0$) light in the MoS_2 monolayer. The absorbance of normal incidence s-polarized light is not shown because it coincides with the absorbance of normal incidence p-polarized light, as is also obvious from Fig. 1. Since all relevant features in absorption spectra correspond to transitions between valence or conducting Mo(d) and valence or conducting S(p) orbitals, such excitations are denoted as Mo(d)↔ S(p) excitations.

We see optical absorption onset at about 1.75 eV and slowly increasing plateau which corresponds to Mo(d)↔ S(p) excitations around the K point. The intensive peak 2.7 eV, denoted as C, corresponds to direct Mo(d)↔ S(p) excitations at point P, as can be seen in Fig. 4. The peak at 3.1 eV, denoted as D, corresponds to transitions between Van Hove singularities at the M point, which exhibits very intensive S(p) character in the valence band and very intensive Mo(d) character in the conduction band. The peak at 3.7 eV, denoted as E, is a result of transitions between the Van Hove singularities in the second valence band [with dominant S(p) character] and the second conduction band [with dominant Mo(d) character] at the M point.

Blue dots in Fig. 5(a) show the experimental results for optical absorption in MoS_2 monolayer [31]. Qualitatively the same experimental result is reported in Ref. [24], but in arbitrary units so it cannot be quantitatively compared with our result. The intensity of experimental peak at 2.85 eV is in excellent agreement with intensity of the C peak. However, the C peak is red-shifted to 2.7 eV. This disagreement is due to the fact that our RPA result does not include electron-hole attraction (which decreases excitation energy) and quasiparticle correction of LDA electronic spectra (which increases excitation energy). The best example of inadequacy of RPA results is the lack of excitonic effect in the vicinity of optical absorption onset. Experimental result shows two peaks (denoted as A and B), corresponding with excitons formed due to the interaction between an excited electron in the lowest conduction band and an excited hole in the spin-orbit (SO) split valence band at the K point. Very sophisticated calculations of optical absorption spectra in MoS_2-ML, which include spin-orbit coupling, quasiparticle GW correction of LDA states, and electron-hole attraction obtained by solving Bethe-Salpeter equation (so-called GW-BSE scheme [21–23]), are presented in [19,20]. All excitonic features obtained in these papers are in very good agreement with available experimental results [7,8,24]. However, here we are looking for the physical origin of highly excited modes C, D, and E in the optical spectra. For that purpose, we implement a different method, two-band TBA model, which is complementary to *ab initio* method in the sense that many of the parameters become more controllable, and the computational effort for each set of parameters is negligible.

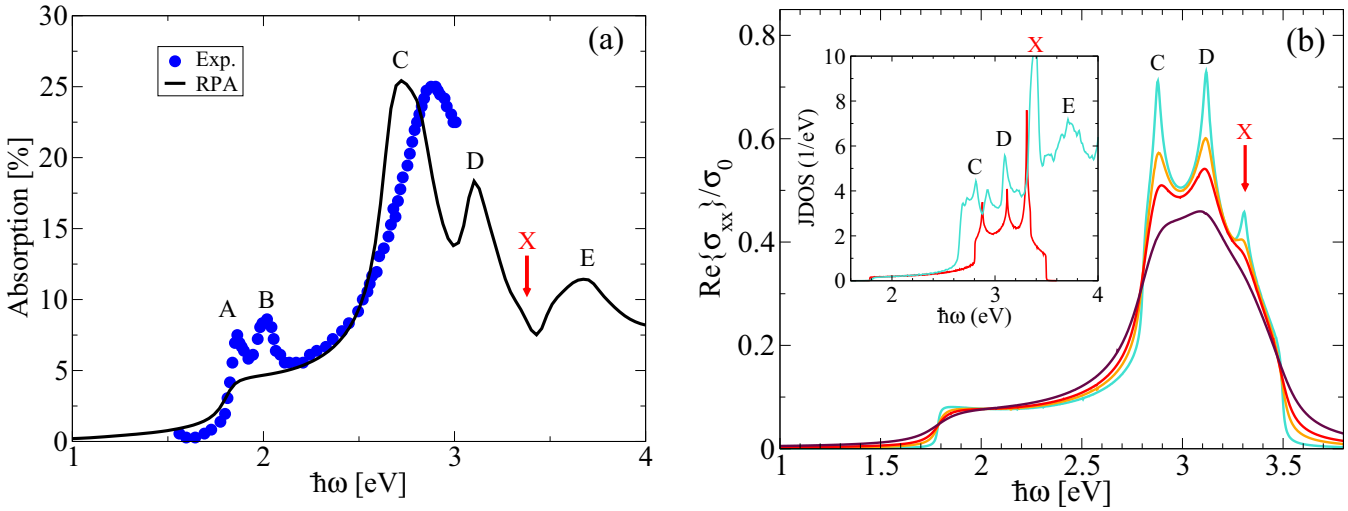

FIG. 5. (a) The optical absorbance of p-polarized normal incidence ($\theta = 0$) light in MoS_2-ML calculated from Eq. (11) (black solid line), the experimental result taken from Ref. [31] (blue dots). (b) Real part of optical conductivity (23) in units of $\sigma_0 = e^2/4\hbar$ with increasing relaxation constant $\hbar\gamma = 10$ meV (turquoise), 30 meV (orange), 50 meV (red), and 100 meV (maroon). The inset shows the *ab initio* JDOS (turquoise) and TBA-JDOS (red).

The blue line in Fig. 5(b) inset represents *ab initio* joint density of states (JDOS)

$$\mathrm{JDOS}(\omega) = \frac{1}{V}\sum_{\substack{\mathbf{K},\sigma \\ L,L'}}[f_L(\mathbf{K}) - f_{L'}(\mathbf{K})] \times \delta[\hbar\omega + E_L(\mathbf{K}) - E_{L'}(\mathbf{K})] \quad (24)$$

in MoS_2-ML. Around the optical absorption onset, the JDOS shows characteristic step function behavior which is a fingerprint of the direct transitions between two-dimensional parabolic bands, as the square-root behavior would be in the three-dimensional case. Optical absorption spectrum in Fig. 5(a), which does not include excitonic effects, shows the same character. Because of the absence of current vertices in JDOS, all electronic excitations are equally permitted, so it could contain extra structure in comparison with absorption spectrum. For example, the JDOS contains X peak, at 3.4 eV, which is missing in absorption spectrum. This issue will be discussed below. The red line in Fig. 5(b) inset represents TBA-JDOS, which is much more refined because of the analytical treatment of two bands and due to the absence of other bands.

The optical conductivity in MoS_2 obtained in the two-band TBA model is shown in Fig. 5(b). We can see that the optical conductivity at energies right above the band gap is by an order of magnitude smaller than the conductivity of doped graphene [37], and about 20 times smaller than the experimental value in MoS_2 [31]. The reason for this discrepancy is in the unrealistically small value of the molybdenum-sulfur hopping parameter t_{sm} used for this calculation, since it can be seen from Appendix D that the interband current vertices are proportional to t_{sm} which is an order of magnitude smaller than interatomic hopping parameter in graphene [38]. Unfortunately, we have to keep this value so small because larger t_{sm} would increase the number of neighbors needed to fit the dispersions significantly. In addition to that, we would also need to include a second-neighbor molybdenum-sulfur hopping. In this approach, which resembles the construction of the TBA Hamiltonian from the Fourier transformation of the valence bands with the constraint of having two orbitals in the unit cell, the calculation of current vertex would become even more complicated than it already is. Since our aim is to show the origin of some significant features in the absorption spectrum like the positions of certain peaks which depend mostly on the properties of the valence bands, we can use the aforementioned two-band model. It will produce an accurate qualitative picture of the optical spectra irrespective of the quantitative disagreement.

In order to clarify why in Fig. 5(a) the nonzero absorption appears below the optical gap energy (long tail below $\hbar\omega = 1.78$ eV) in Fig. 5(b), the TBA absorption (or optical conductivity) is calculated for different relaxation constants $\hbar\gamma$. It can be seen that for $\hbar\gamma = 10$ meV (turquoise) the absorption behaves almost as step function with onset at $\hbar\omega = 1.78$ eV. However, for bigger relaxation constants, e.g., for $\hbar\gamma = 50$ meV (red) which corresponds to damping parameter $\eta = 50$ meV used in *ab initio* calculation, the absorption becomes more dispersive functions with long tail spreading into the energy region below the optical gap, which is exactly how the *ab initio* absorption behaves in Fig. 5(a). Therefore, the finite absorption below the optical gap energy can be attributed to absorption due to various dissipative mechanisms in the system.

For shorter relaxation constants (e.g., for $\hbar\gamma = 10$ and 30 meV), the optical conductivity shows two distinct (pronounced) maxima. The first maximum, denoted as C, originates from the direct transitions between valence and conduction band at point P in the Brillouin zone. P, H, and M and are saddle points, i.e., they represent Van Hove singularities which can be seen as sharp peaks in DOS in Fig. 4. The same transition at P point reflects a C peak in JDOS [Fig. 5(b) inset]. The second maximum, denoted as D, originates from transitions at the M point, which is also manifested as the two most intensive peaks in DOS and as D peak in JDOS. The third, small, maximum at 3.4 eV in Fig. 5(b), denoted as X, is the most intriguing one. Namely, it does not appear in *ab initio* absorption spectra [Fig. 5(a)], but it does appear as the most intensive peak in JDOS, calculated using both methodologies [X peak in Fig. 5(a) inset], and finally there are no Van Hove singularities in DOS (Fig. 4) from which it would originate. It originates from transitions between parallel (holelike) parabolic bands around the Γ point. Even though the DOS of both bands at the Γ point is negligible, the peak is intensive because many equally separated energy levels laying on parallel parabolas contribute to JDOS (which depends on energy difference). Moreover, the X peak in the optical conductivity is highly reduced due to the current vertices (not present in JDOS) which filter just the dipole active transitions. In Fig. 5(b), we can also see that how the relaxation constant increases the X peak decreases, and finally disappears for $\hbar\gamma = 50$ meV. The damping parameter η appearing in *ab initio* current-current response function (B3) corresponds exactly to relaxation constant $\hbar\gamma$ appearing in TBA current-current response function (23). The damping parameter used in *ab initio* calculation is $\eta = 50$ meV, which corresponds to the TBA relaxation constant $\hbar\gamma = 50$ meV when the X peak in Fig. 5(b) disappears, so this explains why the X peak in Fig. 5(a) is also missing. The E peak at 3.7 eV does not appear in the TBA result because it originates from the transition between the higher-order valence and conduction bands, not included in TBA.

B. Angle-resolved optical absorption and transmission in MoS_2 monolayer

Figure 6(a) shows optical absorbance and Fig. 6(b) shows transmittance of p-polarized light in MoS_2 monolayer as function of incident angle θ and photon energy $\hbar\omega$. For normal incidence, i.e., $\theta = 0$ (electrical field is parallel to crystal plane) the absorption spectrum is the same as in Fig. 5(a). It can be noticed that the peaks in absorption spectra coincide with the dips in the transmitted spectra, and that the sum of the two is almost identical to the incident flux. This means that only a negligible part of the incident radiation is reflected. As incident angle increases, the absorption monotonically decreases. For nearly grazing incidence, i.e., $\theta = 80^\circ$ (electrical field is perpendicular to crystal plane), the absorption becomes negligible, i.e., smaller than 1%, and the transmission is almost 100% in the whole

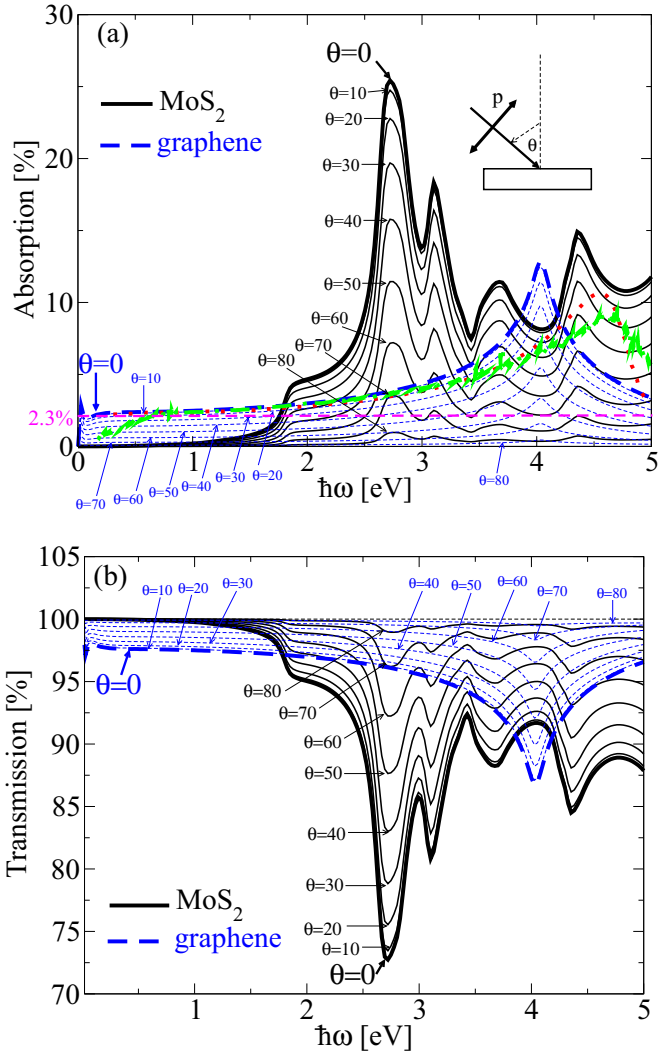

FIG. 6. Angle-resolved optical absorbance (a) and transmittance (b) in MoS_2 monolayer (black lines) and in graphene monolayer (blue dashed lines). The incident angle increases as $\theta_n = n\Delta\theta$; $n = 0,1,\ldots,8$, where $\Delta\theta = 10^\circ$, as denoted in the graphs. Normal incidence ($\theta = 0$) absorbance in graphene taken from Ref. [18] (red dotted line) and Ref. [4] (green dashed-dotted line).

presented photon energy range. This leads to the conclusion that the Mo(d)↔ S(p) transitions represent in-plane charge or current density oscillations which can be excited only with electrical field with nonzero parallel component. In other words, this means that MoS_2 monolayer is completely transparent when it is illuminated with grazing incidence p-polarized light. Presented results are in good qualitative agreement with angle-resolved EELS measurements presented in Figs. 2(a) and 3 of Ref. [39] which demonstrate that EELS spectra decrease as in-plane component of momentum transfer (q_y) increases (which is analogous with increasing incident angle).

It is intriguing that the character of Mo(d)↔ S(p) transitions is intrinsically in plane, even though they represent transitions between Mo(d) orbitals with d_{z^2} and $d_{x^2-y^2}$ character laying in molybdenum plane and S(p) orbitals with p_x and p_y character maximally localized in sulfur planes. Therefore, this kind of transition should also have partially out-of-plane character because sulfur occupies every second site in the honeycomb arrangement and is not positioned directly above molybdenum. However, since there are two sulfur planes, these out-of-plane transitions apparently do not have dipole character, but rather some higher multipole, so they do not couple to external electromagnetic field. Electromagnetic field induces in-plane dipole moment, consisting of transitions between Mo(d) orbitals and (even) linear combination of S(p) orbitals in two sulfur planes with final weight in the molybdenum plane. The same arguments were used to construct our two-band TBA model. Therefore, we can conclude that the MoS_2 modes are quite simple optical modes in visible frequency range, consisting of dipole active charge or current oscillations in the molybdenum plane.

C. Comparison with angle-resolved optical absorption in graphene

The graphene can serve as useful reference for the analysis of the optical properties of other quasi-2D crystals. Here, we briefly analyze the normal incidence optical absorption in pristine graphene obtained in other theoretical and experimental investigations [4,14–18] and its angle-resolved optical absorption in order to emphasize its complementarity to MoS_2-ML.

The thick blue dashed lines in Fig. 6 show the graphene optical absorption for normal incidence ($\theta = 0$). The parameters of calculations are the same as in Ref. [14]. Absorption onset appears already at $\hbar\omega = 0$ which is due to the gapless dipole active $\pi \rightarrow \pi^*$ interband transitions near the K point of the BZ. In the whole infrared (IR) photon energy range ($\hbar\omega < 1.7$ eV), the absorption is close to the universal value of $\pi\alpha = 2.3\%$ (where $\alpha = \frac{1}{137}$ is the fine-structure constant), denoted by the horizontal magenta dashed line, as predicted experimentally in Refs. [15,16]. In the visible photon energy range ($1.7 < \hbar\omega < 3.5$ eV), the absorption monotonically increases. The first absorption maximum, which appears in the ultraviolet (UV) region at $\hbar\omega = 4$ eV, is a consequence of the dipole active interband $\pi \leftrightarrow \pi^*$ transitions along the MM' and $M\Gamma$ directions of the first Brillouin zone, as discussed in detail in [17]. This resonance absorbs about 12% of incident electromagnetic energy. This result agrees well with the theoretical result obtained in Ref. [18] (shown by red dotted line) and the experimental result obtained in Ref. [4] (shown by green dashed-dotted line). However, our RPA absorption maximum shows the same symptoms as the C peak in MoS_2-ML, it is red-shifted (4.05 eV) in comparison with theoretical and experimental peak at 4.62 eV. In Ref. [18], the authors provided full GW-BSE calculation (which includes quasiparticle corrections and electron-hole attraction) and the agreement with the experiment is much better. However, our result is in excellent agreement with the theoretical result in the whole IR and visible photon energy region, which is the region of main future interest. For $\hbar\omega < 0.5$ eV, both theoretical results start disagreeing with the experimental absorption spectrum which suddenly decreases below the universal value. This is probably due to the weak doping which causes a shift of optical absorption onset from $\hbar\omega = 0$ to $\hbar\omega = 2E_F$.

The thin blue dashed lines in Fig. 6(a) show the optical absorbance for larger incident angles ($\theta = 10^\circ$–80°) of p-polarized light in single-layer graphene. It can be seen that the IR and visible photon energy ($\hbar\omega < 3$ eV) plateau, and absorption maximum at 4 eV decrease as the incident angle increases. Blue thick dashed line in Fig. 6(b) shows the normal ($\theta = 0$) and blue thin lines show larger angles ($\theta = 10^\circ$–80°) transmittance in single-layer graphene. Since the reflectivity is negligible (or at least very small) in the presented photon energy range, the transmittance can be obtained as the incident flux reduced by the absorbance. For grazing incidence when absorption becomes negligible the transmittance is almost 100% and graphene is completely transparent. This indicates intrinsically in-plane character of the $\pi \leftrightarrow \pi^*$ transitions in graphene, like the Mo(d)↔ S(p) transitions in MoS_2.

In the visible photon energy range (e.g., from 1.7 to 3.5 eV), where absorption of graphene is minimal and it behaves as almost completely transparent, MoS_2 absorption is maximal. On the other hand, it is well known that pristine graphene behaves as a very good conductor (it has very high dc conductivity) [40]. In addition to that, small doping can enhance graphene dc conductivity, and reduce absorption in the visible frequency range. All this suggests that graphene/MoS_2 composite can potentially be used in photovoltaic devices, where MoS_2 acts as the optically active element (light absorber) and graphene acts as the transparent conductive electrode (or so-called TCO in case of metal oxides), as previously predicted in Ref. [13].

IV. CONCLUSION

The focus of this paper is to explore the physical origin of the most prominent features in MoS_2 optical spectra in visible and near ultraviolet (NUV) photon energy range (1.7–4 eV) by use of recently proposed theoretical tools. We showed that optical spectra consist of three peaks originating from transitions between valence and conducting Mo(d) and S(p) bands. The most intensive C peak, at 2.7 eV, is due to transitions between parabolic bands located between Γ and K points of first Brillouin zone. The D peak, at $\hbar\omega = 3.1$ eV, is due to transitions between Van Hove singularities at the M point. Finally, the E peak, at 3.7 eV, is due to transitions between Van Hove singularities in the second valence and second conduction bands at the M point. The validity of the results is supported by our 2B-TBA model which produced the same results in the visible photon energy range. Calculation of angle-resolved optical absorption and transmission showed that the optical absorbance monotonically decreases, while the transmittance increases, as the incident angle of p-polarized light increases. This implies that the charge or current fluctuations, which produce all features in the spectra, have an in-plane character and that MoS_2 is completely transparent when it is illuminated by nearly grazing incidence p-polarized light. The results are compared with angle-resolved optical absorption and transmission in graphene, and it is shown that MoS_2 reaches maximal absorption in the visible photon energy range, where graphene still behaves as transparent, making these materials suitable for application in solar cells.

ACKNOWLEDGMENTS

The authors thank I. Kupčić for useful discussions and invaluable advice. Computational resources were provided by the DIPC computing center. V.D. acknowledges support from the QuantiXLie Center of Excellence.

APPENDIX A: FREE PHOTON PROPAGATOR

The Fourier transform of free photon propagator can be explicitly written as [25]

$$\hat{\mathbf{D}}^0 = \begin{bmatrix} D^0_{xx} & 0 & 0 \\ 0 & D^0_{yy} & D^0_{yz} \\ 0 & D^0_{zy} & D^0_{zz} \end{bmatrix}, \tag{A1}$$

where

$$D^0_{xx}(Q,\omega,z,z') = \frac{2\pi i}{c\beta} e^{i\beta|z-z'|}, \tag{A2}$$

$$D^0_{yy}(Q,\omega,z,z') = \frac{2\pi i c\beta}{\omega^2} e^{i\beta|z-z'|}, \tag{A3}$$

$$D^0_{zz}(Q,\omega,z,z') = -\frac{4\pi c}{\omega^2}\delta(z-z') + \frac{2\pi i c Q^2}{\beta\omega^2} e^{i\beta|z-z'|}, \tag{A4}$$

and

$$\begin{aligned} D^0_{yz}(Q,\omega,z,z') &= D^0_{zy}(Q,\omega,z,z') \\ &= -\frac{2\pi i c Q}{\omega^2}\mathrm{sgn}(z-z')\, e^{i\beta|z-z'|}, \end{aligned} \tag{A5}$$

where $\beta = \sqrt{\frac{\omega^2}{c^2} - Q^2}$.

APPENDIX B: CURRENT-CURRENT RESPONSE TENSOR

The main quantity appearing in the above expressions for reflectivity, absorbance, and transmittance [Eqs. (10)–(12)] is the current-current response tensor $\Pi_{\mu\nu}$. It describes the microscopic current density fluctuations in the crystal slab. In RPA, it can be obtained by solving the matrix Dyson equation

$$\begin{aligned} \mathbf{\Pi}_{G_z,G'_z}(\mathbf{Q},\omega) = \mathbf{\Pi}^0_{G_z,G'_z}(\mathbf{Q},\omega) + \sum_{G_{z1},G_{z2}} \mathbf{\Pi}^0_{G_z,G_{z1}}(\mathbf{Q},\omega)\mathbf{D}^0_{G_zG'_z}(\mathbf{Q},\omega) \\ \times \mathbf{\Pi}_{G_{z2},G'_z}(\mathbf{Q},\omega), \end{aligned} \tag{B1}$$

where

$$\mathbf{D}^0_{G_z,G'_z}(\mathbf{Q},\omega) = \frac{1}{L}\int_{-L_{uc}/2}^{L_{uc}/2} dz\, dz' e^{-iG_z z}\mathbf{D}^0(\mathbf{Q},\omega,z,z') e^{iG'_z z'}. \tag{B2}$$

We see that the z integration in (B2) is restricted exactly to the $-L_{uc}/2$ to $L_{uc}/2$ interval, which implies that the interaction of the current fluctuation created in the region $-L_{uc}/2 < z < L_{uc}/2$ via photon propagator $\mathbf{D}^0(\mathbf{Q},\omega,z,z')$ is only possible with the current fluctuation in the region $-L_{uc}/2 < z' < L_{uc}/2$, even though the induced electromagnetic field is not limited to that region. This restriction guarantees that $\mathbf{\Pi}$ contains information only about the electromagnetic modes characteristic for the electronic system limited to the region $-L_{uc}/2 < z < L_{uc}/2$ (i.e., q2D systems). The similar restriction is applied in the z integration in (3) which results in "external" field coupling and inducing current fluctuation

only in the region $-L_{uc}/2 < z < L_{uc}/2$. The current-current response tensor of noninteracting electrons can be written as [14]

$$\Pi^0_{\mu\nu,G_z,G'_z}(\mathbf{Q},\omega) = \frac{1}{V}\sum_{\mathbf{K},L,L'} \frac{\hbar\omega}{E_L(\mathbf{K}) - E_{L'}(\mathbf{K}+\mathbf{Q})} \times \left[J^{\nu}_{\mathbf{K}L,\mathbf{K}+\mathbf{Q}L'}(G'_z)\right]^* J^{\mu}_{\mathbf{K}L,\mathbf{K}+\mathbf{Q}L'}(G_z) \times \frac{f_L(\mathbf{K}) - f_{L'}(\mathbf{K}+\mathbf{Q})}{\hbar\omega + i\eta + E_L(\mathbf{K}) - E_{L'}(\mathbf{K}+\mathbf{Q})}, \tag{B3}$$

where the current vertices are

$$J^{\mu}_{\mathbf{K}L,\mathbf{K}+\mathbf{Q}L'}(G_z) = \int_{\Omega} d\mathbf{r}\, e^{-i\mathbf{Q}\cdot\boldsymbol{\rho} - iG_z z} J^{\mu}_{\mathbf{K}L,\mathbf{K}+\mathbf{Q}L'}(\mathbf{r}), \tag{B4}$$

and where

$$J^{\mu}_{\mathbf{K}L,\mathbf{K}+\mathbf{Q}L'}(\mathbf{r}) = \frac{\hbar e}{2im}\{\phi^*_{L\mathbf{K}}(\mathbf{r})\partial_\mu \phi_{L'\mathbf{K}+\mathbf{Q}}(\mathbf{r}) - [\partial_\mu \phi^*_{L\mathbf{K}}(\mathbf{r})]\phi_{L'\mathbf{K}+\mathbf{Q}}(\mathbf{r})\}. \tag{B5}$$

Here, $V = S \times L_{uc}$ is the normalization volume, S is the normalization surface, and $f_L(\mathbf{K}) = (e^{[E_L(\mathbf{K})-E_F]/k_BT}+1)^{-1}$ is the Fermi-Dirac distribution at temperature T. Integration in (B4) is performed over the normalization volume Ω. Plane-wave expansion of the wave function has the form

$$\Phi_{L\mathbf{K}}(\boldsymbol{\rho},z) = \frac{1}{\sqrt{\Omega}} e^{i\mathbf{K}\cdot\boldsymbol{\rho}} \sum_{\mathbf{G}} C_{L\mathbf{K}}(\mathbf{G}) e^{i\mathbf{G}\cdot\mathbf{r}},$$

where the coefficients $C_{L\mathbf{k}}$ are obtained by solving the KS equations self-consistently and $\mathbf{G} = (G_x, G_y, G_z)$ are 3D reciprocal lattice vectors.

APPENDIX C: PEIERLS SUBSTITUTION

Peierls substitution in the bare Hamiltonian is defined as follows:

$$\begin{aligned}\hat{H}_0 &= \sum_{\mathbf{R},\boldsymbol{\delta}}\sum_{\ell\ell'} H_0^{\ell\ell'}(\boldsymbol{\delta}+\mathbf{r}_{\ell'\ell}) c^\dagger_{\mathbf{R}\ell} c_{\mathbf{R}+\boldsymbol{\delta}\ell'} \\ &\to \sum_{\mathbf{R},\boldsymbol{\delta}}\sum_{\ell\ell'} H_0^{\ell\ell'}(\boldsymbol{\delta}+\mathbf{r}_{\ell'\ell}) c^\dagger_{\mathbf{R}\ell} c_{\mathbf{R}+\boldsymbol{\delta}\ell'} \\ &\quad \times \exp\left\{\frac{ie}{\hbar c}\int_{\mathbf{R}+\boldsymbol{\delta}+\mathbf{r}_{\ell'}}^{\mathbf{R}+\mathbf{r}_\ell} d\mathbf{s}\,\mathbf{A}(\mathbf{s},t)\right\} = \hat{H}_{\rm tot}.\end{aligned} \tag{C1}$$

In the long-wavelength limit, the vector potential varies negligibly between the two neighbors separated by $\boldsymbol{\delta}$, and the integral can be approximated by the midpoint rule:

$$\int_{\mathbf{R}+\boldsymbol{\delta}+\mathbf{r}_{\ell'}}^{\mathbf{R}+\mathbf{r}_\ell} d\mathbf{s}\,\mathbf{A}(\mathbf{s},t) \approx -(\boldsymbol{\delta}+\mathbf{r}_{\ell'\ell})\cdot\mathbf{A}\left(\mathbf{R}+\frac{\boldsymbol{\delta}}{2}+\bar{\mathbf{r}},t\right) \tag{C2}$$

with $\bar{\mathbf{r}} = (\mathbf{r}_\ell + \mathbf{r}_{\ell'})/2$. Interacting Hamiltonian is defined and obtained to the linear order in vector potential

$$\begin{aligned}\hat{H}^{\rm ext} &= \hat{H}_{\rm tot} - \hat{H}_0 \\ &\approx -\frac{ie}{\hbar c}\sum_{\substack{\mathbf{R},\boldsymbol{\delta}\\ \ell,\ell'}} (\boldsymbol{\delta}+\mathbf{r}_{\ell'\ell})\cdot\mathbf{A}\left(\mathbf{R}+\frac{\boldsymbol{\delta}}{2}+\bar{\mathbf{r}},t\right) \\ &\quad \times H^{\ell\ell'}(\boldsymbol{\delta}+\mathbf{r}_{\ell'\ell}) c^\dagger_{\ell\mathbf{R}} c_{\ell'\mathbf{R}+\boldsymbol{\delta}}.\end{aligned}$$

Using momentum representation of the fermion operators and vector potential

$$c^\dagger_{\mathbf{R}\ell} = \sum_{\mathbf{K}} e^{-i\mathbf{K}\cdot(\mathbf{R}+\mathbf{r}_\ell)} c^\dagger_{\ell\mathbf{K}}, \quad \mathbf{A}(\mathbf{r},t) = \sum_{\mathbf{Q}} e^{i\mathbf{Q}\cdot\mathbf{r}}\mathbf{A}(\mathbf{Q},t),$$

and defining

$$H^{\ell\ell'}\left(\mathbf{K}+\frac{\mathbf{Q}}{2}\right) = \sum_{\boldsymbol{\delta}} H^{\ell\ell'}(\boldsymbol{\delta}+\mathbf{r}_{\ell'\ell}) e^{i(\mathbf{K}+\frac{\mathbf{Q}}{2})\cdot(\boldsymbol{\delta}+\mathbf{r}_{\ell\ell'})}, \tag{C3}$$

we get

$$\hat{H}^{\rm ext} = -\frac{1}{c}\sum_{\mathbf{Q},\mu} A_\mu(\mathbf{Q},t)\sum_{\mathbf{K},\ell\ell'}\frac{e}{\hbar}\frac{\partial H^{\ell\ell'}\left(\mathbf{K}+\frac{\mathbf{Q}}{2}\right)}{\partial k_\mu} c^\dagger_{\ell\mathbf{K}+\mathbf{Q}} c_{\ell'\mathbf{K}}.$$

Evidently, the paramagnetic current operator is

$$\hat{J}^{\rm para}_\mu(-\mathbf{Q}) = \sum_{\mathbf{K},\ell\ell'}\frac{e}{\hbar}\frac{\partial H^{\ell\ell'}\left(\mathbf{K}+\frac{\mathbf{Q}}{2}\right)}{\partial K_\mu} c^\dagger_{\ell\mathbf{K}+\mathbf{Q}} c_{\ell'\mathbf{K}}. \tag{C4}$$

APPENDIX D: CURRENT VERTEX

We define a Bloch creation operator in tight-binding approximation

$$c^\dagger_{L\mathbf{K}} = \sum_{\ell} U_{\mathbf{K}}(L,\ell) c^\dagger_{\ell\mathbf{K}}. \tag{D1}$$

The sum $\sum_\ell$ extends over all orbitals in the unit cell participating in the valence bands, and the $U_{\mathbf{K}}(L,\ell)$ are elements of the transformation matrix between delocalized orbital representation and the diagonal one, which can be obtained by solving the Schrödinger equation

$$\sum_{\ell'} U_{\mathbf{K}}(L,\ell')[H^{\ell\ell'}(\mathbf{K}) - E_L(\mathbf{K})\delta_{\ell\ell'}] = 0. \tag{D2}$$

After introducing notation

$$\begin{aligned}\varepsilon_{ms}(\mathbf{K}) &= \varepsilon_m(\mathbf{K}) - \varepsilon_s(\mathbf{K}), \quad \tan\theta(\mathbf{K}) = \frac{2|t(\mathbf{K})|}{\varepsilon_{ms}(\mathbf{K})}, \\ t(\mathbf{K}) &= |t_{sm}(\mathbf{K})|e^{i\varphi(\mathbf{K})}, \quad \tan\varphi(\mathbf{K}) = \frac{t_i(\mathbf{K})}{t_r(\mathbf{K})},\end{aligned} \tag{D3}$$

where $t_i(\mathbf{K}) = \mathrm{Im}\, t(\mathbf{K})$ and $t_r(\mathbf{K}) = \mathrm{Re}\, t(\mathbf{K})$, the transformation matrix is

$$U_{\mathbf{K}}(L,\ell) = \begin{pmatrix} e^{-i\varphi(\mathbf{K})}\cos\frac{\theta(\mathbf{K})}{2} & -\sin\frac{\theta(\mathbf{K})}{2} \\ e^{-i\varphi(\mathbf{K})}\sin\frac{\theta(\mathbf{K})}{2} & \cos\frac{\theta(\mathbf{K})}{2}\end{pmatrix}.$$

We can now verify that the inverse representation is given by

$$c^\dagger_{\ell\mathbf{K}} = \sum_L U_{\mathbf{K}}(\ell,L) c^\dagger_{L\mathbf{K}}. \tag{D4}$$

To evaluate the current vertex in (C4) in long wave limit ($\mathbf{Q} = 0$), we use (D4) and get

$$J_{\mu}^{LL'}(\mathbf{K}) = \sum_{\ell\ell'} \frac{e}{\hbar} \frac{\partial H^{\ell\ell'}(\mathbf{K})}{\partial K_{\mu}} U_{\mathbf{K}}(\ell, L) U_{\mathbf{K}}^{*}(\ell', L).$$

By noting that

$$\frac{\partial \varphi(\mathbf{K})}{\partial K_{\mu}} = \frac{1}{|t(\mathbf{K})|^2} \left\{ t_r(\mathbf{K}) \frac{\partial t_i(\mathbf{K})}{\partial K_{\mu}} - t_i(\mathbf{K}) \frac{\partial t_r(\mathbf{K})}{\partial K_{\mu}} \right\}, \quad \text{(D5)}$$

$$\frac{\partial \theta(\mathbf{k})}{\partial K_{\mu}} = \frac{(2/\varepsilon_{ms}(\mathbf{K}))}{1 + \tan^2\theta(\mathbf{K})} \left\{ \frac{\partial |t(\mathbf{K})|}{\partial K_{\mu}} - \frac{\tan\theta(\mathbf{K})}{2} \frac{\partial \varepsilon_{ms}(\mathbf{K})}{\partial K_{\mu}} \right\} \quad \text{(D6)}$$

for the interband case, we obtain

$$J_{\mu}^{PM}(\mathbf{K}) = \frac{e}{\hbar} \left(\frac{E_{PM}(\mathbf{K})}{2} \frac{\partial \theta(\mathbf{K})}{\partial K_{\mu}} + i |t(\mathbf{K})| \frac{\partial \varphi(\mathbf{K})}{\partial K_{\mu}} \right),$$

where $E_{PM}(\mathbf{K}) = E_{+}(\mathbf{K}) - E_{-}(\mathbf{K})$ is the difference between the energy eigenvalues.

[1] K. Novoselov, D. Jiang, F. Schedin, T. Booth, V. Khotkevich, S. Morozov, and A. Geim, Proc. Natl. Acad. Sci. USA **102**, 10451 (2005).

[2] Wu Hua-Qiang, Linghu Chang-Yang, L Hong-Ming, and Qian He, Chin. Phys. B **22**, 098106 (2013).

[3] F. Bonaccorso, Z. Sun, T. Hasan, and A. C. Ferrari, Nat. Photon. **4**, 611 (2010).

[4] Kin Fai Mak, Long Ju, Feng Wang, and Tony F. Heinz, Solid State Commun. **152**, 1341 (2012).

[5] T. Low and P. Avouris, ACS Nano **8**, 1086 (2014).

[6] V. Despoja, I. Lončarić, D. J. Mowbray, and L. Marušić, Phys. Rev. B **88**, 235437 (2013).

[7] A. Splendiani, L. Sun, Y. Zhang, T. Li, J. Kim, C. Y. Chim, G. Galli, and F. Wang, Nano Lett. **10**, 1271 (2010).

[8] K. F. Mak, C. Lee, J. Hone, J. Shan, and T. F. Heinz, Phys. Rev. Lett. **105**, 136805 (2010).

[9] N. G. Chopra, R. J. Luyken, K. Cherrey, V. H. Cresp, M. L. Cohen, S. G. Louie, and A. Zettl, Science **269**, 966 (1995).

[10] J. S. Lauret, R. Arenal, F. Ducastelle, A. Loiseau, M. Cau, B. Attal-Tretout, E. Rosencher, and L. Goux-Capes, Phys. Rev. Lett. **94**, 037405 (2005).

[11] Yong-Nian Xu and W. Y. Ching, Phys. Rev. B **44**, 7787 (1991).

[12] A. K. Geim and I. V. Grigorieva, Nature (London) **499**, 419 (2013).

[13] M. Bernardi, M. Palummo, and J. C. Grossman, Nano Lett. **13**, 3664 (2013).

[14] D. Novko, M. Šunjić, and V. Despoja, Phys. Rev. B **93**, 125413 (2016).

[15] R. R. Nair, P. Blake, A. N. Grigorenko, K. S. Novoselov, T. J. Booth, T. Stauber, N. M. R. Peres, and A. K. Geim, Science **320**, 1308 (2008).

[16] Kin Fai Mak, Matthew Y. Sfeir, Yang Wu, Chun Hung Lui, James A. Misewich, and Tony F. Heinz, Phys. Rev. Lett. **101**, 196405 (2008).

[17] D. Novko, V. Despoja, and M. Šunjić, Phys. Rev. B **91**, 195407 (2015).

[18] L. Yang, J. Deslippe, C.-H. Park, M. L. Cohen, and S. G. Louie, Phys. Rev. Lett. **103**, 186802 (2009).

[19] D. Y. Qiu, F. H. da Jornada, and S. G. Louie, Phys. Rev. Lett. **111**, 216805 (2013).

[20] A. Molina-Sanchez, D. Sangalli, K. Hummer, A. Marini, and L. Wirtz, Phys. Rev. B **88**, 045412 (2013).

[21] L. Hedin, Phys. Rev. **139**, A796 (1965).

[22] G. Strinati, Phys. Rev. B **29**, 5718 (1984).

[23] M. Rohlfing and S. G. Louie, Phys. Rev. Lett. **81**, 2312 (1998).

[24] K. P. Dhakal, D. L. Duong, Jubok Lee, Honggi Nam, Minsu Kim, Min Kan, Y. Hee Leea, and Jeongyong Kim, Nanoscale **6**, 13028 (2014).

[25] V. Despoja, M. Šunjić, and L. Marušić, Phys. Rev. B **80**, 075410 (2009).

[26] P. Giannozzi, S. Baroni, N. Bonini, M. Calandra, R. Car, C. Cavazzoni, D. Ceresoli, G. L. Chiarotti, M. Cococcioni, I. Dabo *et al.*, J. Phys.: Condens. Matter **21**, 395502 (2009).

[27] C. Hartwigsen, S. Goedecker, and J. Hutter, Phys. Rev. B **58**, 3641 (1998); S. Goedecker, M. Teter, and J. Hutter, *ibid.* **54**, 1703 (1996).

[28] J. P. Perdew and A. Zunger, Phys. Rev. B **23**, 5048 (1981).

[29] H. J. Monkhorst and J. D. Pack, Phys. Rev. B **13**, 5188 (1976).

[30] T. Cao, G. Wang, W. Han, H. Ye, C. Zhu, J. Shi, Q. Niu, P. Tan, E. Wang, B. Liu, and J. Feng, Nat. Commun. **3**, 887 (2012).

[31] Yilei Li, A. Chernikov, X. Zhang, A. Rigosi, H. M. Hill, Arend M. van der Zande, Daniel A. Chenet, En-Min Shih, J. Hone, and Tony F. Heinz, Phys. Rev. B **90**, 205422 (2014).

[32] E. Cappelluti, R. Roldan, J. A. Silva-Guillen, P. Ordejon, and F. Guinea, Phys. Rev. B **88**, 075409 (2013).

[33] E. Ridolfi, D. Le, T. S. Rahman, E. R. Mucciolo, and C. H. Lewenkopf, J. Phys.: Condens. Matter **27**, 365501 (2015).

[34] I. Kupčić, Phys. Rev. B **90**, 205426 (2014).

[35] A. Konar, R. Jana, T. Fang, G. Li, W. O'Brien, and D. Jena, arXiv:1109.5145.

[36] R. Peierls, Z. Phys. **80**, 763 (1933).

[37] Z. Q. Li, E. A. Henriksen, Z. Jiang, Z. Hao, M. C. Martin, P. Kim, H. L. Stormer, and D. N. Basov, Nat. Phys. **4**, 532 (2008).

[38] S. Reich, J. Maultzsch, C. Thomsen, and P. Ordejon, Phys. Rev. B **66**, 035412 (2002).

[39] J. Hong, Kun Li, Chuanhong Jin, X. Zhang, Ze Zhang, and Jun Yuan, Phys. Rev. B **93**, 075440 (2016).

[40] I. Kupčić, Phys. Rev. B **91**, 205428 (2015).